doi:10.20944/preprints202203.0212.v1

Corrosion resistance of Fe-contaminated Al-Si-Cu-Zn alloys modified with Ni and Co and with variable secondary dendrite arm spacing

Marcella G. C. Xavier [1], Brenda J. M. Freitas [1], Guilherme Y. Koga [1,2] and José E. Spinelli [1,2,*]

[1] Federal University of São Carlos, Graduate Program in Materials Science and Engineering, 13565-905 - São Carlos, SP, Brazil.
[2] Department of Materials Engineering, Federal University of São Carlos - UFSCar, 13565-905 - São Carlos, SP, Brazil.
* Correspondence: spinelli@ufscar.br;

Abstract: The corrosion behavior of Fe-containing directionally solidified (DS) and centrifugally cast (CC) Al-Si-Cu-Zn alloys with either Co or Ni additions has been investigated. Electrochemical and immersion corrosion methods were used to investigate the corrosion behavior in 0.6 M NaCl after short (1-hour) and long (30-day) exposure periods. The employed solidification methods allowed the production of samples with a wide range of secondary dendrite arm spacing (SDAS) while preserving Si and Fe-containing phases. The 0.5 wt.% Ni and Co additions led to the growth of the AlFeSi(Ni) and AlFeSi(Co) phases, but no binary AlNi nor AlCo intermetallic particles have been generated. Potentiodynamic polarization studies at early exposure revealed an increase in the corrosion potential as the Ni was added for either fast or slow solidified samples. The electrochemical impedance spectroscopy at early exposure demonstrated that the Ni-modified alloy, on the other hand, was associated to smaller charge transfer resistances, indicating a reduction in corrosion resistance after short elapsed time into the electrolyte. However, 30-day immersion tests revealed much lower corrosion rate of the Ni-modified alloy than the other alloys, while the corrosion rates of the Co-modified and non-modified alloys were similar. In the Ni-containing alloy, decreased corrosion rate under long-term corrosion process was attributed to the formation of a thick and dense alumina layer, effectively protecting the surface under such conditions. This work contributes to a better knowledge of the corrosion behavior of Ni- and Co-corrected Al industrial scrap compositions.

Keywords: Corrosion; Solidification; Dendritic growth; Al-Si-Fe alloys; Modification, Intermetallics.

1. Introduction

Addition of alloying elements is an effective manner to improve and control properties of Al alloys. If maintained in solid solution, some alloying elements increase the corrosion resistance [1–3]. This is because the precipitates may act as cathodes for the preferential corrosion of the α-Al matrix [4].

In Al alloys, impurities such as Fe and Si establish cathodic phases regarding to the α-Al matrix, whose shape, size, and distribution affect and harm the corrosion properties of the α-Al phase [5,6]. Local loss in passivity is reported to occur in the vicinity of the second phases, resulting in localized corrosion along the interfaces. It has been reported that the structural characteristics of the film and the severity of the corrosion attack may be influenced by (*i*) the chemical composition of the exposed alloys, (*ii*) the presence and distribution of micro, macro-defects, and second phases and (*iii*) the electrolyte composition [5–7].

Al and its alloys exposed to aggressive environments, especially those containing chloride ions (Cl^-), are sensitive to pitting corrosion [8]. The effects of adding Ni to Al-Si alloys immersed in NaCl solution have been evaluated in some previous studies [9–13]. Hypereutectic Al-Si-Fe-Cu-Zn alloys containing either Ni or Ni/Cr were evaluated and compared through weight loss experiments in 3.5 wt.% NaCl electrolyte [9]. A higher thickness loss values within the first three days of exposure were associated to the Ni-containing alloy.. However, as the elapsed time increased (> 3 days), the corrosion rate reduced considerably. Following corrosion testing, scanning electron microscopy (SEM) and energy-dispersive x-ray spectroscopy (EDX) investigations were conducted. A layer of Al oxide and hydroxide corrosion products was formed on the surface. Although interesting results were furnished, after the test has been completed, no strategy has been devised for eliminating corrosion products and, as a result, analyzing the corrosion damage that has occurred on the underneath Al alloy.

Hossain et al. [10] evaluated the resistance to corrosion of the Al-6Si-0.5Mg alloy modified with 2 wt.% Ni in 0.1 M NaCl. It was found that the corrosion current density (i_{corr}) and corrosion rate (CR) were reduced as compared to the non-modified alloy, as assessed from linear polarization resistance and potentiodynamic polarization tests. The Ni addition to the Al-6Si-0.5Mg alloy altered the open circuit potential (OCP) at the steady-state, corrosion potential (E_{corr}), and pitting corrosion potential (E_{pit}) towards more positive potential values. In contrast, the addition of Co up to 0.5 wt.% to Al-Si-Fe alloys in HCl solution contributed to an increase in corrosion resistance in both tested conditions: as-cast and age-hardened specimens [11].

Mirzaee-Moghadam et al. [12] doped the Al-Si piston alloy with different Ni contents (0.8%, 2%, 2.6%, and 3.5 wt.%) to investigate corrosion properties for samples subjected to the 3.5 wt.% NaCl solution. The presence of Ni-bearing intermetallic compounds decreased the corrosion rate by 60%. Nevertheless, the repassivation potential was observed to be greater in the 2.6% Ni-containing sample, indicating that micropits repassivated more easily due to the Ni additions. Arthanari and coauthors [13] investigated the corrosion behavior of high pressure die-cast Al-Si-Ni alloys (Al-3Si-1Ni and Al-3Si-3Ni) in 3.5 wt.% NaCl solution. The lower amount of Al_3Ni phase was responsible for the better corrosion resistance of the Al-3Si-1Ni alloy. The growth of a stable corrosion product layer mostly composed of $Al(OH)_3/Al_2O_3$ on the surface was linked to the reduction in the amount of hydrogen developed as the immersion period was extended. This layer reduced the mobility of aggressive ions from penetrating deeper into the system, improving corrosion resistance.

Processing route to which a material is subjected is closely linked to its final properties, including electrochemical ones [14–16]. The secondary dendrite arm spacing (SDAS) is considered the main technical feature used to evaluating casting alloys and their properties. The effects of SDAS on the corrosion behavior of Al-Si alloys has been reported [14]. For the Al-9wt.%Si alloy subjected to the laser surface remelting process, the microstructural modification provided a reduction of SDAS in about five times compared the SDAS of an as-cast sample. The significant microstructural refinement was observed to decrease the corrosion resistance due the susceptibility of a high number of boundaries between the α-Al phase and the Si particles.

Since the addition of correctors such as Ni and Co intends to benefit a greater number of process conditions and applications, evaluating corrosion associated with different microstructural scales becomes an indispensable task. It is also interesting to note that studies with Ni additions, although existing, remain scarce and contradictory, especially due to the non-observation of stable potentials before electrochemical tests.

This study evaluates the Al-7wt.%Si alloy with low levels of impurities, including 0.35 wt.%Cu, 0.25 wt.%Zn and 0.6 wt.%Fe, typical of industrial Al scraps [17]. The Al-7wt.%Si alloy and its modified versions (Ni and Co) have been subjected to two different processes: directional solidification (DS) and centrifugal casting (CC). The purpose is to gain insight into the influence of chemical composition (Ni, Co additions), and dendritic microstructure scale on the corrosion behavior of both as-cast specimen conditions for samples exposed to the 0.6 M NaCl solution. Weight loss immersion tests and electrochemical methods were utilized to assess information on the corrosion behavior at early (1-hour) and long (30-day) exposures to 0.6 M NaCl solution, in addition to microstructure characterization for determining SDAS and intermetallics characterizing the samples.

2. Materials and Methods

Three alloys were considered: i) Al-7%Si-0.6%Fe-0.35%Cu-0.25%Zn, ii) Al-7%Si-0.6%Fe-0.35%Cu-0.25%Zn-0.5%Co, and iii) Al-7%Si-0.6%Fe-0.35%Cu-0.25%Zn-0.5%Ni. They were manufactured from commercial pure elements (>99.7%), and characterized and tested in the "as-cast" conditions. The Co and Ni levels were chosen based on the suitable contents for the correction of Fe-contaminated Al alloys, as stated in the literature [15,18,19]. Two different processing methods were employed to induce distinct dendritic microstructure refinements: directional solidification (slow) and copper mold centrifugal casting (fast solidification). Therefore, SDAS was adopted as a control parameter so that the size of the dendritic network could be translated.

Commercially pure Al was induction melted and maintained for 20 minutes at approximately 800 °C in a SiC crucible prior to the insertion of Si, Fe, Cu, Co and Ni elements to the molten bath. Zn was the last element to be added given its low melting point. To favor alloy homogeneity, the molten alloy was kept in the induction furnace for at least 40 minutes. All alloys were Ar-degassed (before pouring) for two minutes to minimize porosity.

The molten alloy was poured into a stainless-steel cylindrical mold coupled to the directional solidification furnace (Manufacturer: Fortelab Indústria de Fornos Elétricos Ltda-ME, São Carlos, Brazil). The internal surface of the mold was previously coated with alumina, and the water-cooled mold's base was covered with a sheet made of SAE 1020 steel. Molten temperature was controlled through radial electrical wire. The electrical cable was unplugged after the nearest thermocouple from the cooled base indicated 5% above the alloy *liquidus* temperature. Thermal analysis was previously used to establish the *liquidus* temperatures. Finally, the water-cooling system began to extract heat in a single direction. This is due to heat extraction from the water cooling system at the mold's bottom base, which promotes upward directional solidification [16,20].

A portion of the directionally solidified (DS) castings was utilized to make centrifugally cast (CC) samples. These samples were produced by centrifugal copper-mold using a Linn High Therm induction furnace, model Titancast 700 VAC. Three distinct plate mold thicknesses were used in the chamber to make pieces attaining 2 mm, 3 mm and 4 mm. The microstructures of these CC alloy samples were investigated and compared to those of the DS alloys.

The samples were chosen to focus on the variance of Fe-containing intermetallics under slow and fast solidification regimes: SDAS of approximately 21 μm for the DS samples and of approximately 5 μm for the CC samples of the three alloys. Other features within each kind of processing, such as the Si spacing, which correspondingly follows the SDAS size as shown schematically in Figure 1, were examined, and may be regarded constant. For alloys within each processing, the intermetallic proportion remained almost constant. When comparing the differences across processing methods, a difference in the length-scale of the phases may be seen as will be discussed later.

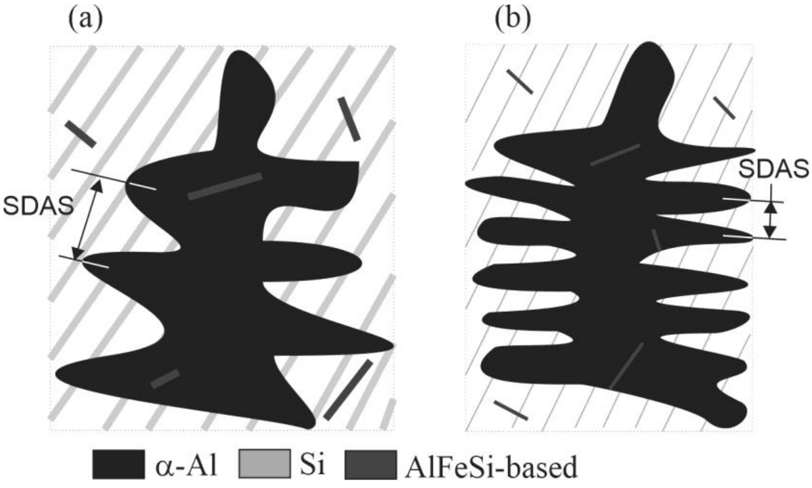

Figure 1. Schematic representation of the *α*-Al dendritic arrangements, Si and IMCs for (a) slow and (b) fast solidified samples used in the present analysis.

The samples were sanded, polished, and etched as needed to reveal the resulting microstructures for analysis [21]. An optical microscope was used to investigate the specimen's dendritic microstructures (Olympus Corporation, GX41 model, Tokyo, Japan). The measuring technique described by Gündüz and Çadirli [22] was considered to calculate SDAS values. Furthermore, a scanning electron microscopy (SEM) was employed to register greater magnification images before and after corrosion as well as compositions/morphologies of the generated phases (Philips XL30 FEG equipped with a XFlash 6|60 SDD EDS, Eindhoven, The Netherlands).

For corrosion tests, 1200# abrasive papers were used to wet grind both 21-µm-SDAS and 5-µm-SDAS samples. They were cleaned with anhydrous ethanol and washed with distilled water before testing.

The corrosion resistance of the Al-Si-Fe-Cu-Zn (-Co, and -Ni) alloys at different as-cast conditions was evaluated using electrochemical impedance spectroscopy (EIS) and potentiodynamic polarization tests in a chloride-rich solution. The working electrodes were the DS and CC samples (exposed area of 0.4 cm^2), the counter electrode was a platinum grid, and the reference electrode was a saturated calomel electrode (SCE) using a traditional three-electrode cell setup and a Gamry 600+ potentiostat (Gamry instruments, PA, USA). The electrolyte was a naturally aerated chloride-rich solution, 0.6 M NaCl, pH 5.5, made using demineralized water and high purity NaCl reagent (>99 percent). The tests were conducted in triplicate at ambient temperature and exposed to the air.

The samples were exposed to the electrolyte, and the open circuit potential (OCP) registered for 1 hour, at the end of which a stable potential value ranges were found. After 1-hour at open circuit, EIS tests started using a frequency of 100 kHz to 10 mHz, and a sinusoidal perturbation of 10 mVrms around -20 mV *vs* OCP. Non-linear behavior was found for some Al-alloys at anodic portion of the AC perturbation when tested after early stages of immersion in sodium chloride solution [23], so taken an cathodic potential of -20 mV *vs* OCP has been reported as effective to ensure linearity, as further validated in [24–26]. Following the EIS testing, the samples were exposed to an open circuit condition for 10 minutes to ensure that the corroding system could attain the potential values range prior to EIS. The potentiodynamic polarization measurements were completed in the last phase at 1 mV/s scan rate towards the anodic direction, commencing at a potential of -300 mV below OCP and terminating at +300 mV above OCP.

The corrosion potential (E_{corr}) was determined from polarization curves (Log i *vs* E). EIS data were interpreted from the equivalent electrical circuit (ECC) approach, where the impedance of the selected ECC was fitted to those of the experimentally-obtained, considering the frequency range between 100 kHz and 10 mHz. The Chi-square value (χ^2) was used to determine the EIS data's goodness-of-fit to the EEC, which is the total of the square of the differences between theoretical and experimental data.

Immersion tests of specimens having known initial weight were carried out at room temperature so that corrosion rates using the weight loss method could be determined for all alloys and conditions, as described in [27]. The surface areas of the standardized samples were exposed to a corrosive environment of a 0.6 M NaCl solution inside a container for 30 days. To avoid extraneous particles, the container was kept closed. At the completion of the test, the samples were cleaned with nitric acid (HNO_3) for 2 minutes at room temperature for removing corrosion products [27]. To examine the shape/nature of the corrosion layers that developed on the sample's surface, SEM and X-ray diffraction (XRD) analyses were carried out. The X-ray diffraction data of the CC samples were collected on a Bruker D8 Advance ECO diffractometer under using Cu Kα (λ= 1.54056 Å). Two 2-theta selections have been performed, which complied a specific 15-45º range to decode either the phases of interest or oxides/hydroxides.

3. Results and discussions

3.1. SDAS and secondary phases under slow and fast solidification

Figure 2 displays the microstructures highlighting how the size (scale) of the dendritic arrangement varies as a function of the cooling rate (fast and slow solidification) and elemental additions (Ni or Co). Lower cooling rates related to the DS samples (from left to right micrographs) result in an increase of SDAS of approximately 4 times regardless of the alloy composition. These spectra of solidification rates are essential since they are comparable to those seen in industrial processes such as die-casting, permanent mold, and lost wax casting [28,29]. Furthermore, it appears that adding Co and Ni separately to the Al-7wt.%Si alloy has no effect on the dendritic microstructure length-scale. Microstructures like those in Figure 2 were used to quantify the SDAS following the methods proposed by Gündüz and Çadirli [22].

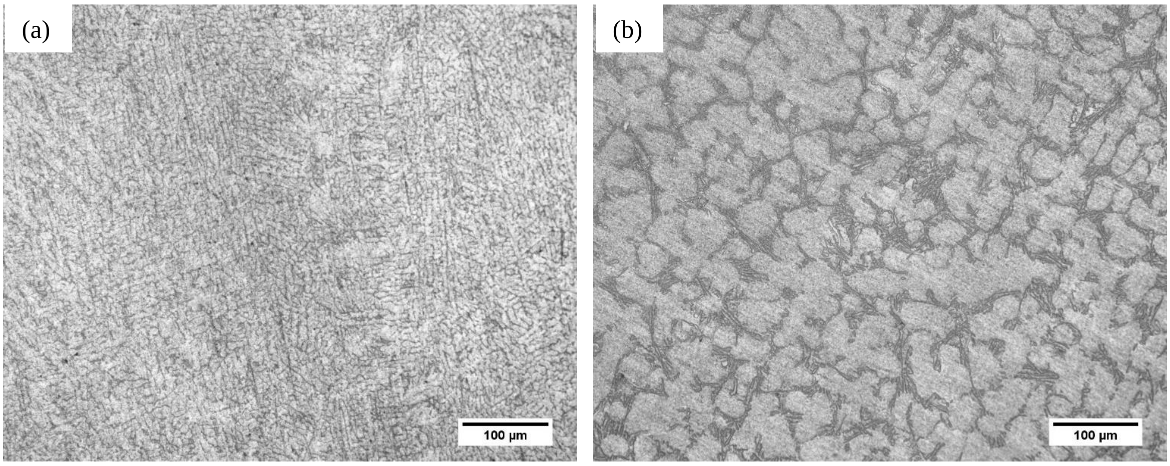

Fast - Non-modified 3C (λ_2=4.9µm) Slow - Non-modified 10mm (λ_2=21.25µm)

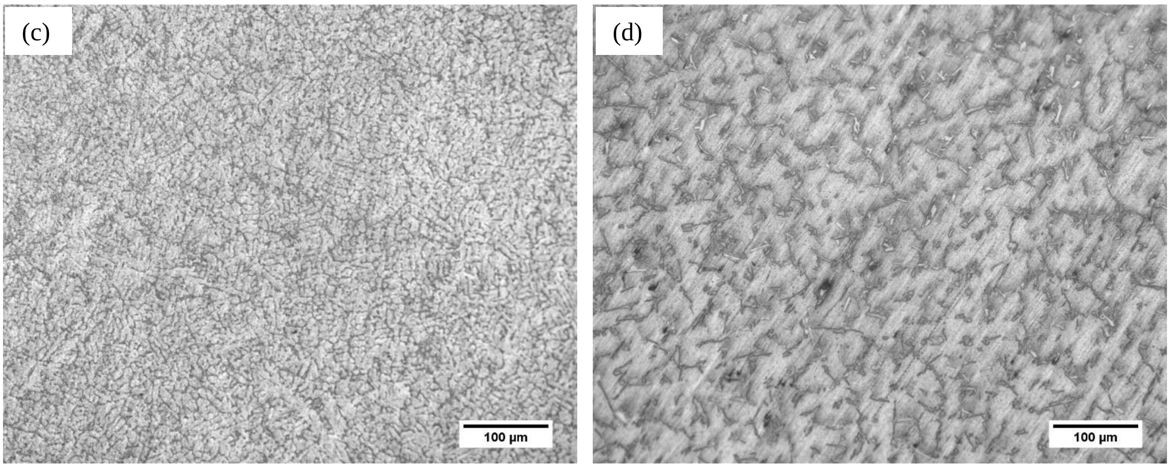

Fast - Ni-containing 2C (λ_2=5.61µm) Slow - Ni-containing 15mm (λ_2=21.12µm)

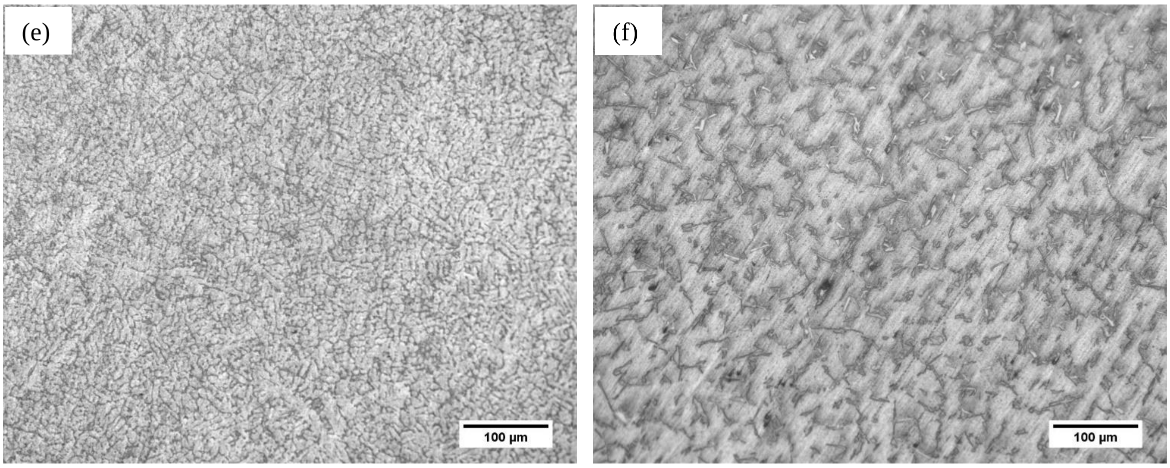

Fast - Co-containing 4B (λ_2=5.28µm) Slow - Co-containing 5mm (λ_2=21.08µm)

Figure 2. Optical micrographs related to the Al-Si-Fe-Cu-Zn (-Co, -Ni) alloys processed under (a,c,e) fast and slow (b,d,f) cooling conditions.

Figure 3 shows SEM images of CC samples that exhibit fine Fe-based and Si phases. The growth of fine intermetallics is related with shorter distances between SDAS, which is quite expected. The DS samples showed the same secondary phases with larger sizes. Such phases are poorly dispersed within the α-Al matrix, being characterized with sharp edges. Some of the Fe-based intermetallics have a Chinese letter morphology [30]. Even with relatively high cooling rates and dendritic fineness of the CC samples, well-distributed particles with a more rounded shape could not be observed [15]. In sum, the microstructures were constituted by an α-Al dendritic matrix, Si and AlFeSi / AlFeSi(Ni) /

AlFeSi(Co) phases. Si is found in solution within the α-Al matrix whereas the other elements are not.

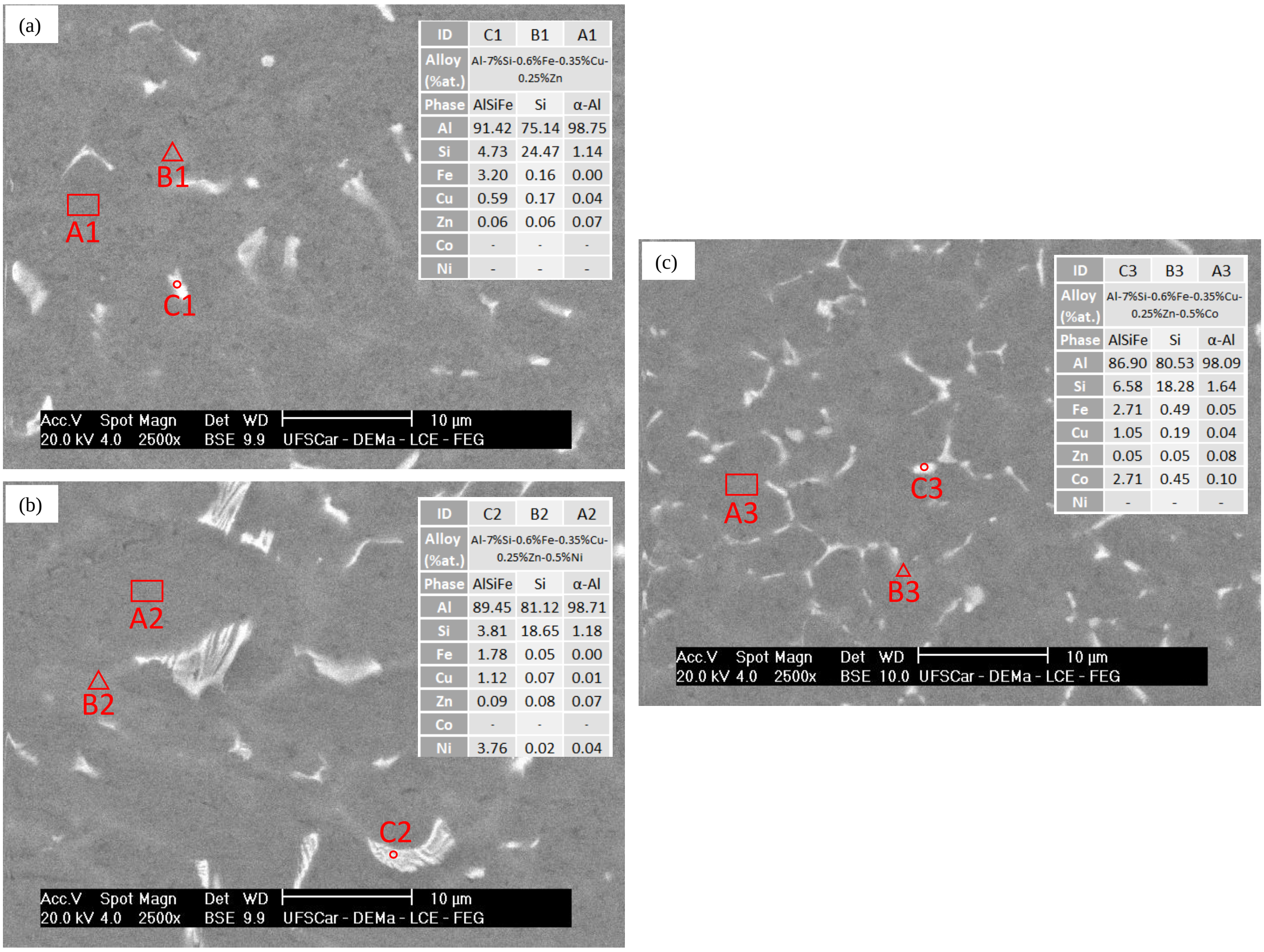

(a)

ID	C1	B1	A1
Alloy (%at.)	Al-7%Si-0.6%Fe-0.35%Cu-0.25%Zn		
Phase	AlSiFe	Si	α-Al
Al	91.42	75.14	98.75
Si	4.73	24.47	1.14
Fe	3.20	0.16	0.00
Cu	0.59	0.17	0.04
Zn	0.06	0.06	0.07
Co	-	-	-
Ni	-	-	-

(b)

ID	C2	B2	A2
Alloy (%at.)	Al-7%Si-0.6%Fe-0.35%Cu-0.25%Zn-0.5%Ni		
Phase	AlSiFe	Si	α-Al
Al	89.45	81.12	98.71
Si	3.81	18.65	1.18
Fe	1.78	0.05	0.00
Cu	1.12	0.07	0.01
Zn	0.09	0.08	0.07
Co	-	-	-
Ni	3.76	0.02	0.04

(c)

ID	C3	B3	A3
Alloy (%at.)	Al-7%Si-0.6%Fe-0.35%Cu-0.25%Zn-0.5%Co		
Phase	AlSiFe	Si	α-Al
Al	86.90	80.53	98.09
Si	6.58	18.28	1.64
Fe	2.71	0.49	0.05
Cu	1.05	0.19	0.04
Zn	0.05	0.05	0.08
Co	2.71	0.45	0.10
Ni	-	-	-

Figure 3. Typical SEM microstructures and EDS analyses for: (a) Al-7%Si-0.6%Fe-0.35%Cu-0.25%Zn, (b) Al-7%Si-0.6%Fe-0.35%Cu-0.25%Zn-0.5%Ni and (c) Al-7%Si-0.6%Fe-0.35%Cu-0.25%Zn-0.5%Co alloys.

3.2. Potentiodynamic polarization

The potentiodynamic polarization curves of the three alloys processed by DS and CC are shown in Figure 4. The polarization curves of the DS alloys, Figure 4a, were similar, characterized by a remarkable increase of the current density even at small anodic polarization. Also, slopes of the cathodic branches were quite similar, suggesting that the kinetics of the cathodic reaction were insensitive to the Co or Ni additions. Besides these similarities, the corrosion potential values were also comparable. However, the currents associated to the E_{corr}, i.e. the corrosion current density (i_{corr}), appear to be the highest for the Ni-containing alloy (black curve), and the lowest for the non-modified alloy (green curve). The polarization curves in Figure 4a do not allow a precise determination of i_{corr} from Tafel extrapolation but a view at E_{corr} clearly indicates that the i_{corr} is likely to be located at superior values between 10^{-6} and 10^{-5} A/cm^2.

For the CC processed alloys, the same overall trends found in the DS ones persisted, as seen in Figure 4b The Ni-containing alloy, despite showing the noblest E_{corr} value, displayed the highest i_{corr} as assessed visually in Figure 4b. Among the tested alloys, the Ni-containing alloys seem to depict the lowest resistance against anodic polarization, given the faster increase of the current density for a same anodic polarization from E_{corr}. The CC non-modified and Co-containing alloys presented a slightly superior resistance against anodic polarization compared to their DS processed equivalent samples. However, it is still without a clear and extended current density plateau along the anodic polarization.

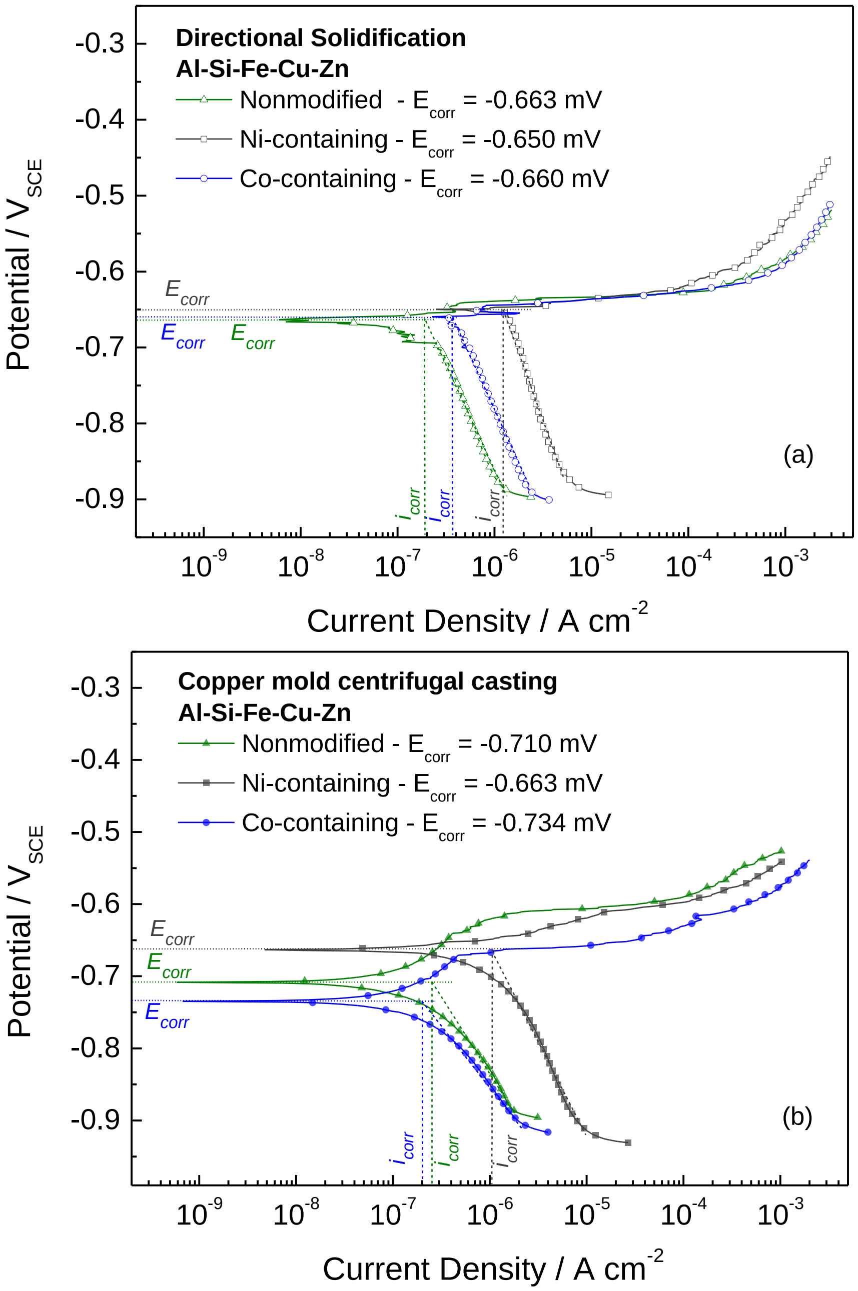

Figure 4. Potentiodynamic polarization curves for the Al-Si-Fe-Cu-Zn (-Co, -Ni) alloy samples having different SDAS: approximately (a) 21 µm (b) 5 µm. Linear cathodic branch along about 1-decade of current in potential values sufficient far from E_{corr} was used for estimation of i_{corr}. Such estimation of i_{corr} intended for comparative purposes among the alloys in this study rather than as a definitive and accurate indication of the corrosion kinetics.

After potentiodynamic polarization experiments associated with short elapsed period in the chloride solution, the surface after testing could be mapped using SEM as a function of large and fine SDAS. Figure 5 displays typical surface characteristics identified on both the CC [Figures 5a), b) and c)] and DS [Figures 5d), e) and f)] samples. Owing to their cathodic action, the Si and Fe-containing phases dissolved the α-Al areas in contact with them. Moreover, the Si phase and Fe-based intermetallics were remained at the interdendritic zones.

Damage appears to be more aggravated for the CC samples. As the whole microstructure is refined as well as the formed interdendritic phases, the α-Al matrix dissolution increased generating a higher number of pittings, as seen in Figures 5a), b) and c). Comparable corrosion morphologies may be seen for the various alloy compositions examined through each process.

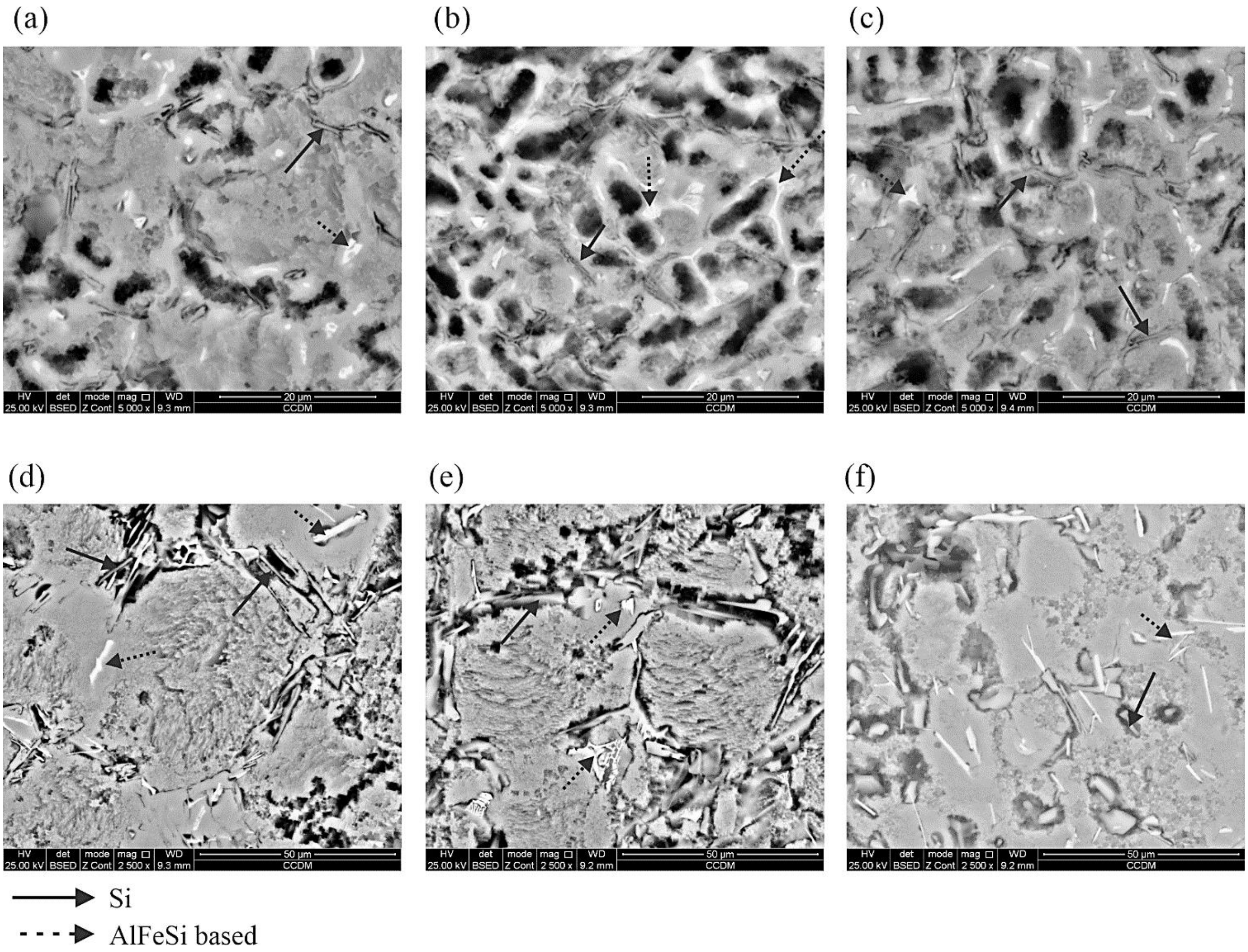

Figure 5. SEM images after potentiodynamic polarization tests for smaller SDAS samples of the (a) Al-7%Si-0.6%Fe-0.35%Cu-0.25%Zn, (b) Al-7%Si-0.6%Fe-0.35%Cu-0.25%Zn-0.5%Ni and (c) Al-7%Si-0.6%Fe-0.35%Cu-0.25%Zn-0.5%Co alloys; and for larger SDAS samples of the (d) Al-7%Si-0.6%Fe-0.35%Cu-0.25%Zn, (e) Al-7%Si-0.6%Fe-0.35%Cu-0.25%Zn-0.5%Ni and (f) Al-7%Si-0.6%Fe-0.35%Cu-0.25%Zn-0.5%Co alloys.

3.3. Electrochemical Impedance Spectroscopy

Figures 6 and 7 show the EIS Nyquist and Bode plots. The Nyquist plots confirmed the presence of two depressed capacitive loops, as also reported by Arthanari et al. [13] for Al-Si-Ni-Cu alloys. Moreover, the Ni-containing alloy's capacitive loop diameters decreased as compared to the other alloys, indicating lower corrosion resistance. The Al-7%Si-0.6%Fe-0.35%Cu-0.25%Zn, Al-7%Si-0.6%Fe-0.35%Cu-0.25%Zn-0.5%Co alloys followed a similar pattern, although the capacitive loop sizes were larger than that related to the Ni-containing alloy samples.

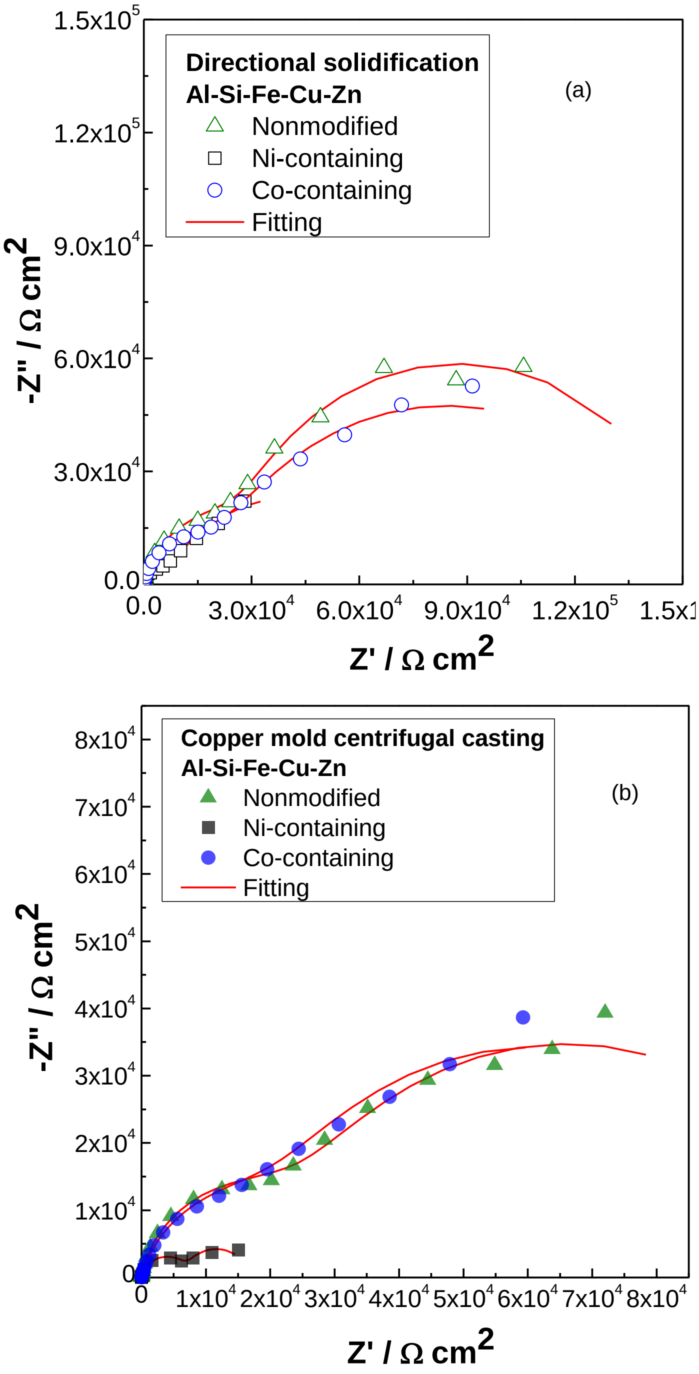

Figure 6. Nyquist plots related to the Al-Si-Fe-Cu-Zn (-Co, -Ni) alloy samples having different SDAS: approximately (a) 21 µm (b) 5 µm.

Two peaks occurred in the phase angle plots as can be seen in Figure 7b, and the phase angle limits and peak areas decreased for Ni-containing alloy samples as compared to the others, indicating least capacitive behavior. Moreover, the modulus of impedance IZI values of the Ni-containing alloy samples also decreased if compared to the other alloys, showing their inferior corrosion resistances.

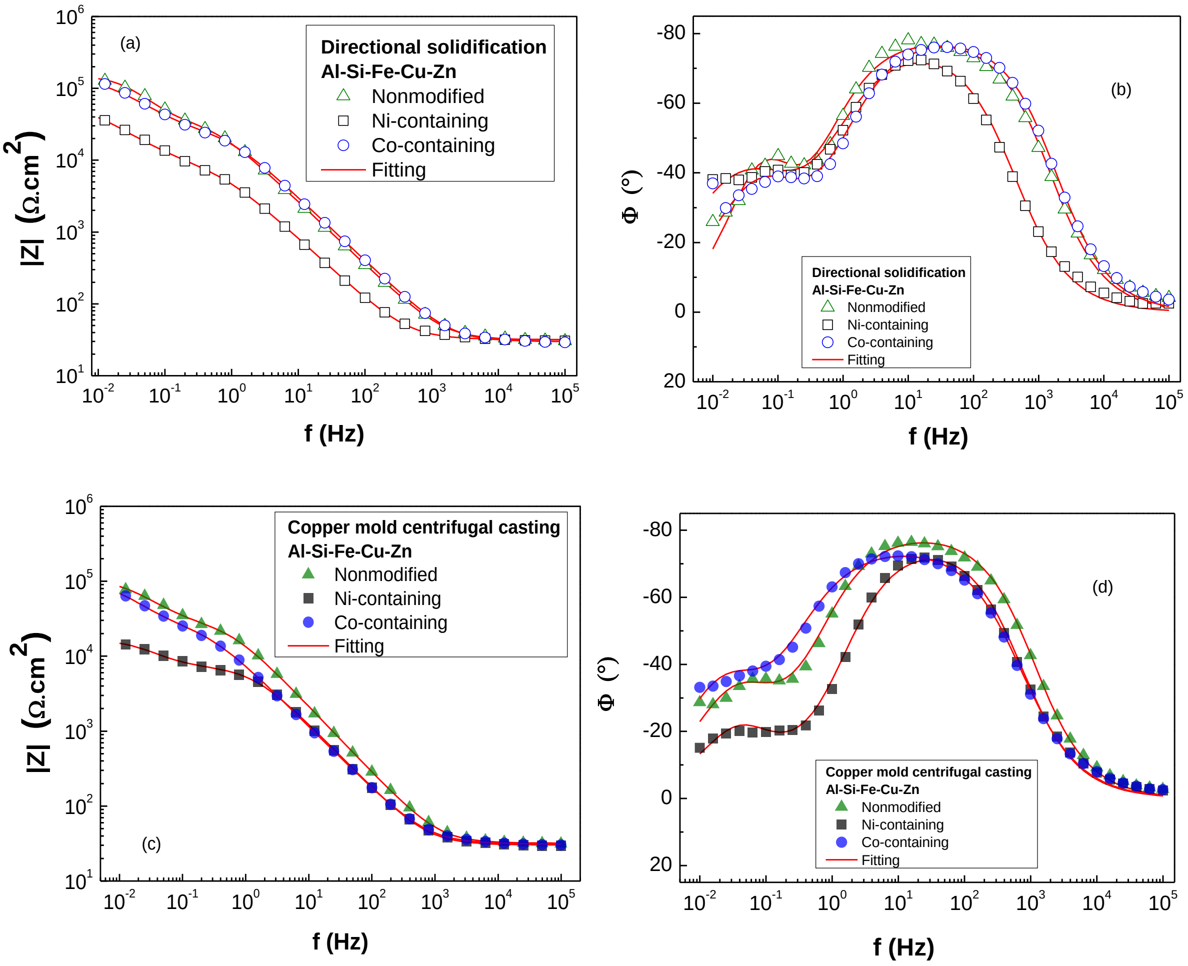

Figure 7. Bode and Bode-phase plots related to the Al-Si-Fe-Cu-Zn (-Co, -Ni) alloy samples having different SDAS: approximately (a,b) 21μm (c,d) 5 μm.

The fitted equivalent circuit (EC) adopted here is illustrated in Figure 8 [31], while the fitted parameters are provided in Table 1. EC curve fitting analyses were performed for all alloy EIS data. The experimental findings correspond well with the estimated values, and the error (χ^2) values are in the acceptable order of 10^{-2}. The EC was composed of : R_s (solution resistance), R_f (surface layer resistance), and R_{ct} (charge transfer resistance), as well as constant phase elements (CPE) of the surface layer (CPE_f) and double layer (CPE_{dl}), being CPE characterized by its Q and α parameters.

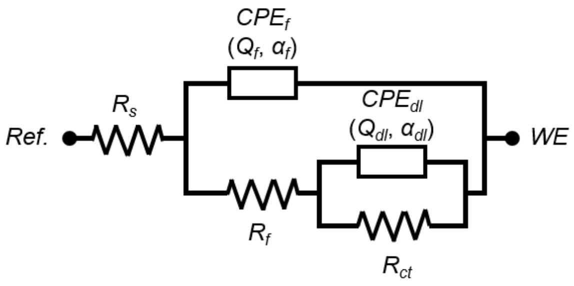

Figure 8. Equivalent electrical circuit used to model the experimental EIS data of the Al-Si-Fe-Cu-Zn (-Co, -Ni) alloys [32–34].

As shown in Table 1, the R_f values of the non-modified, Co- and Ni-containing alloys were 45.9, 30.4, and 10.0 kΩ.cm² for the DS samples, respectively. For the CC samples, 31.7, 31.7, and 7.6 kΩcm² were determined for the same sequence of alloys. These findings revealed that the surface layer produced on the surface during electrolyte exposure contributed to the decrease in corrosion resistance of the Ni-containing alloy. Interestingly, the DS alloys exhibited higher R_f values compared to the alloys CC processed alloys, attributed to the presence of larger Si phase and Fe-based intermetallics, decreasing the microgalvanic coupling areas between these particles and the α-Al matrices.

Charge transfer resistance (R_{ct}) values were found to be 100.9, 111.3 and 67.3 kΩ.cm^2 and 69.7, 62.7 and 9.4 kΩ.cm^2 for the non-modified, Co- and Ni-modified alloys considering DS and CC samples respectively. The Ni-modified alloy exhibited approximately 1.5 and 7.4 times lower R_{ct} values compared to the alloy without modification, confirming its worst corrosion resistance. The difference in R_{ct} between the Co-containing and the non-modified alloys was insignificant.

The EIS results, Figure 7, agree with those from potentiodynamic polarization, Figure 4, both pointing out to the Ni deleterious role regarding the corrosion response after short immersion period (1-hour). The assumption that the corrosion will proceed at constant rate may be misleading for alloys that develop protective layer for long exposure time to the electrolyte. Indeed, the different corrosion behaviors at early- and long-exposure time to the corroding electrolyte are often the source of controversial conclusion about the effect of a given alloying element to the Al alloys.

Table 1. Impedance parameters obtained from the fitting of the EIS data for the Al-Si-Fe-Cu-Zn (-Co, -Ni) alloys in 0.6 M NaCl solution.

Alloys	**Solidification severity**	**SDAS (μm)**	**R_s (Ω cm^2)**	**R_f (kΩ cm^2)**	**Q_f (μF s $^{(\alpha f-1)}$)**	**α_f**	**R_{ct} (kΩ cm^2)**	**Q_{dl} (μF s $^{(\alpha dl-1)}$)**	**α_{dl}**	**χ^2/|Z|**
Non-modified	Slow cooling	21.2	31.6	45.9	4.3	0.84	100.9	14.4	0.98	0.09
Ni-containing	Slow cooling	21.1	31.7	10.0	13.7	0.86	67.3	56100	0.72	0.09
Co-containing	Slow cooling	21.1	29.8	30.4	3.3	0.88	111.3	18.4	0.84	0.04
Non-modified	Fast cooling	4.9	31.9	31.7	4.7	0.88	69.7	33.3	0.88	0.07
Ni-containing	Fast cooling	5.6	30.3	7.3	8.6	0.87	9.4	219.0	0.86	0.09
Co-containing	Fast cooling	5.3	31.1	31.7	10.7	0.85	62.7	51.5	0.88	0.05

3.4. Immersion corrosion results

Electrochemical analyzes (short term) showed that the addition of Ni was detrimental to the corrosion resistance while the other two alloys showed similar results. That is, the Co addition did not affect the corrosion behavior determined by polarization and EIS. These results should be considered with caution, since they reflect the first stage of the corrosion process under the enforced parameters, as detailed in the last Section. There is no electrochemical approach that can be used alone as an accelerated test for evaluating Al alloys [35]. The findings of electrochemical studies must be compared to those of traditional tests, such as weight loss experiments, for instance. This sort of test has allowed assessing the performance of Al alloys in a variety of environments and conditions. To supplement the current findings, immersion corrosion experiments were carried out for 30 days to determine the corrosion rates of all examined alloys.

In Figure 9, macroscopic images of the sample surfaces after 30 days of immersion in 0.6 M NaCl with and after the cleaning procedure aiming corrosion products removal are compared. After 30 days in 0.6 M NaCl solution, the corrosion product surface layer can be seen covering the surface of all alloys. Before removal procedure, white corrosion products were less identified for the Ni-containing alloy, being concentrated in a vertical center line aligned with the sample hole. In the rest of the sample surfaces a more uniform grayish layer was observed as indicated by the arrows in Figure 9.

As also observed by Kaiser et al. [9], the white products were identified as being "mushroom-type" layers. The active dissolution of the alloy resulted in $Al(OH)_3$, which is insoluble in water, and precipitates as a white gel with gelatinous flake aspect [35]. The gray layer related to the Ni-containing alloy in Figure 9 appears to have a nature other than the hydroxide gel. More details about this structure will be seen later.

After cleaning, the samples were weighed to be compared to the masses before immersion. Figure 10 shows the resulting corrosion rates. The weight loss of the alloy containing Ni is much lower as compared to the others, while some mass gain related to the CC samples could be observed. The formation of protective and dense layer on the surface of the Ni-containing samples may be the cause of this slight weight gain. This layer worked as a corrosion barrier, severely reducing the corrosion rate. It should be noted that a tiny portion of the corrosion products were not eliminated for the Ni-containing alloy, however this did not affect the mass measurement results when compared to the other alloys. In other words, the corrosive rate was indeed significantly lower for the alloy with Ni, as assessed after 30-day exposure. In their immersion tests, Kaiser et al. [9] observed an inversion of the behavior of the Al alloy containing Ni. While the alloy containing Ni had a greater corrosion rate for shorter periods (1 to 3 days), it demonstrated a lower corrosion rate for longer elapsed times. This is consistent with what is reported in the current study when the results through the electrochemical and the 30-day immersion tests are compared to each other.

Under these long-term corrosion exposure conditions, it appears that neither the addition of Co nor the scale of the dendritic microstructure has significant impacts on the corrosion rate. However, theNi-containing alloys exhibited an unusual behavior.

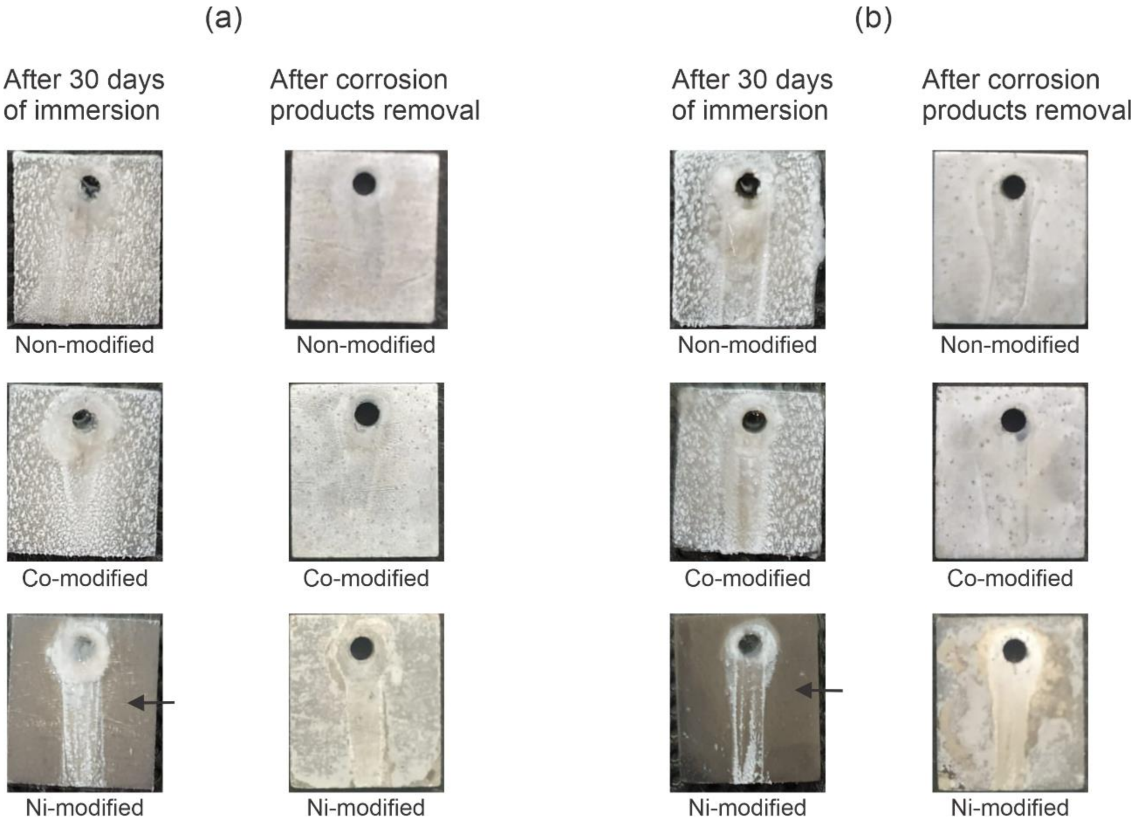

Figure 9. Macroscopic images of (a) DS and (b) CC Al-7%Si-0.6%Fe-0.35%Cu-0.25%Zn, Al-7%Si-0.6%Fe-0.35%Cu-0.25%Zn-0.5%Co and Al-7%Si-0.6%Fe-0.35%Cu-0.25%Zn-0.5%Ni alloys after 30 days of immersion tests.

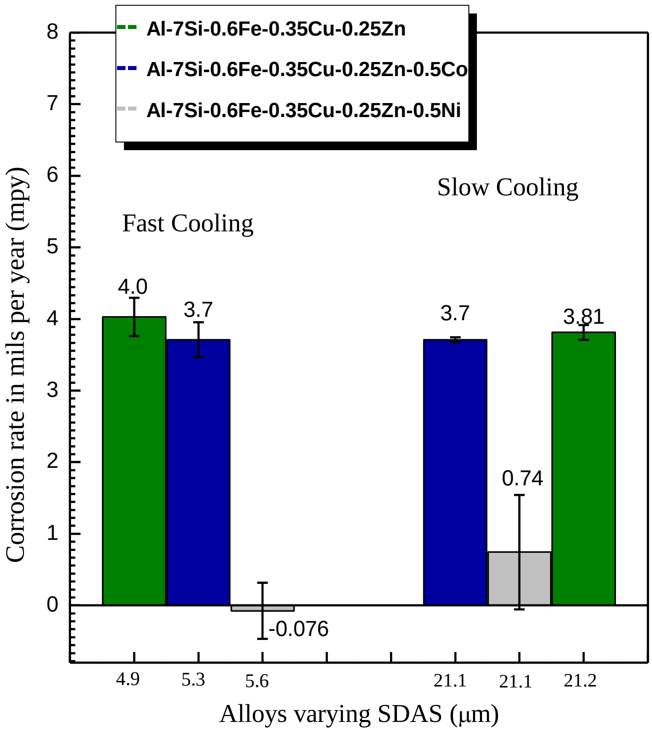

Figure 10. Corrosion rates (mils per year) of the Al-7%Si-0.6%Fe-0.35%Cu-0.25%Zn (-Ni, -Co) samples after 30 days immersed in a 0.6 M NaCl solution.

XRD results were analyzed for the three rapid solidified alloy samples subjected to the 30-day immersion corrosion. In the case of the alloy with Ni, the central position (white area) and periphery (gray area) were examined through separate spectra. All results confirmed the formation of the $Al(OH)_3$. Aside from the phases that constitute the alloy structures, all spectra revealed the existence of Al_2O_3 oxides in the protective layers that had been formed. Formation of corrosion products often displayed an outer hydroxide layer and an inner oxide layer at the alloy's surface, being the latter formed from further oxidation of hydroxides. Oxides are recognized to present a more dense and percolated structure more effective to restrain the ingress of corrosive species towards the active bare surface of the alloy, being desirable as protective layer than hydroxides and oxyhydroxides.

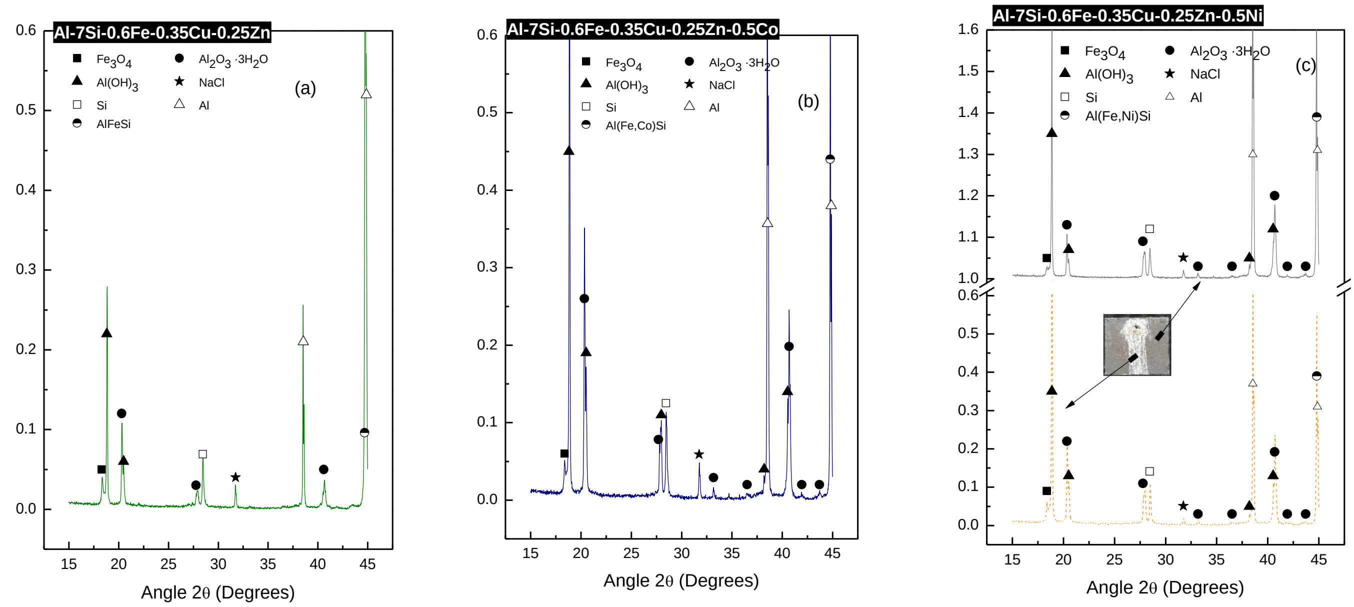

Figure 11. XRD patterns of the alloys solidified at higher cooling rates (CC samples): (a) Al-7%Si-0.6%Fe-0.35%Cu-0.25%Zn, (b) Al-7%Si-0.6%Fe-0.35%Cu-0.25%Zn-0.5%Co and (c) Al-7%Si-0.6%Fe-0.35%Cu-0.25%Zn-0.5%Ni.

The details of stable oxide layers (areas indicated by arrows in Figure 9) mostly composed of Al_2O_3 on the surface for the alloy containing Ni may be seen in Figure 12 and Figure 13. According to the results from Arthanari et al. [31], the generation of this type of structure may be associated to the reduction in the amount of hydrogen developed as the immersion period was extended for the Ni-containing alloys. This prevents aggressive ions from penetrating deeper into the system, improving corrosion resistance. It appears that Ni addition could provide reduced hydrogen volume, suggesting its positive role as modifying element. Indeed, the cathodic reactions that generates gases play an important role to the development and integrity of protective layers on alloys [36]. Reducing the rate of hydrogen developed underneath the protective layer prevents its severe and continuous spalling, favoring thickening and conversion of corrosion products into oxides.

Because the secondary phases are nobler than the α-Al phase, they function as cathodes speeding up the dissolution of the α-Al matrix, as can be seen in the corroded regions highlighted in Figure 12. The α-Al dissolution is quite evident. CC and DS samples showed comparable corrosion morphologies, with selective dissolution of the α-Al phase verified, and secondary phases mostly unaffected, continuing to occupy their sites in the interdendritic regions.

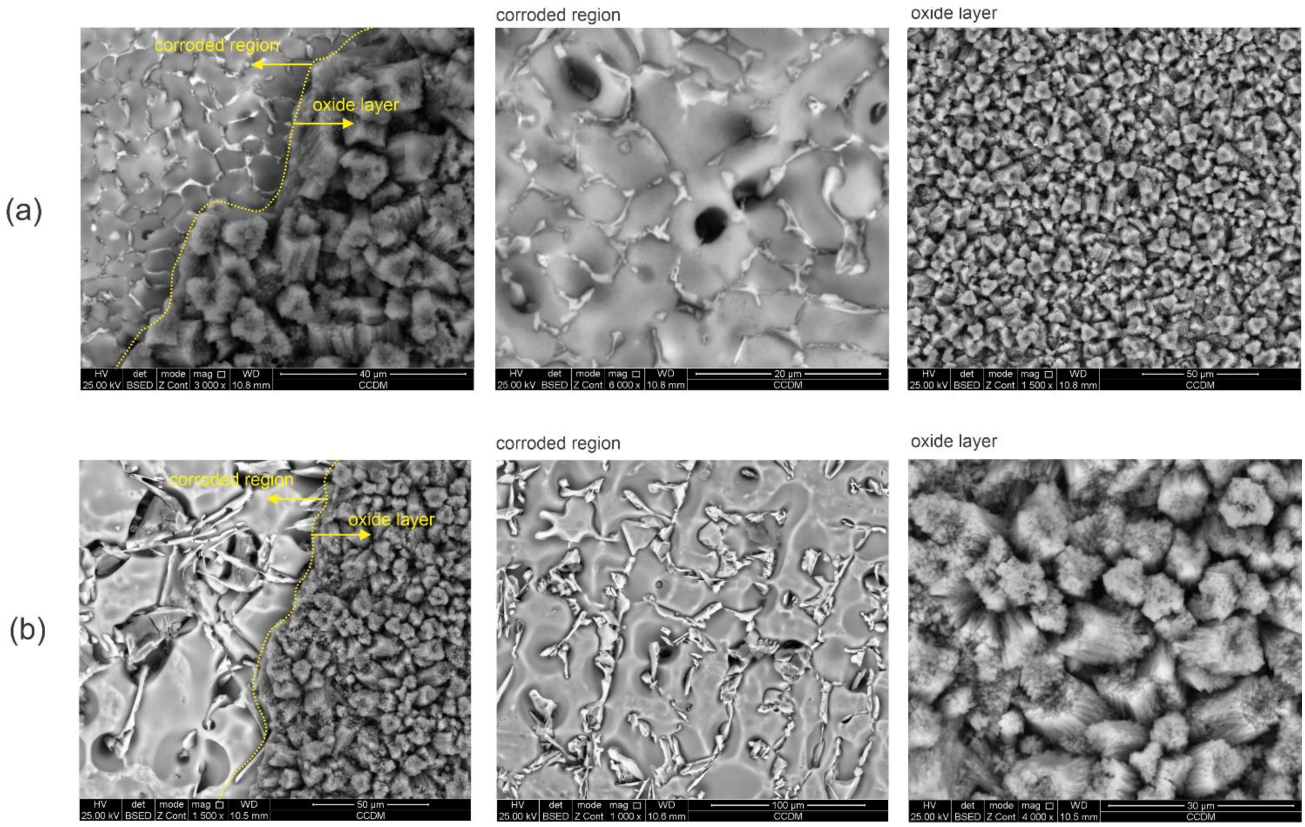

Figure 12. SEM images detailing either corroded or oxide layer regions formed after 30-day immersion experiments with the (a) CC and (b) DS Al-7%Si-0.6%Fe-0.35%Cu-0.25%Zn-0.5%Ni alloy samples in 0.6 M NaCl.

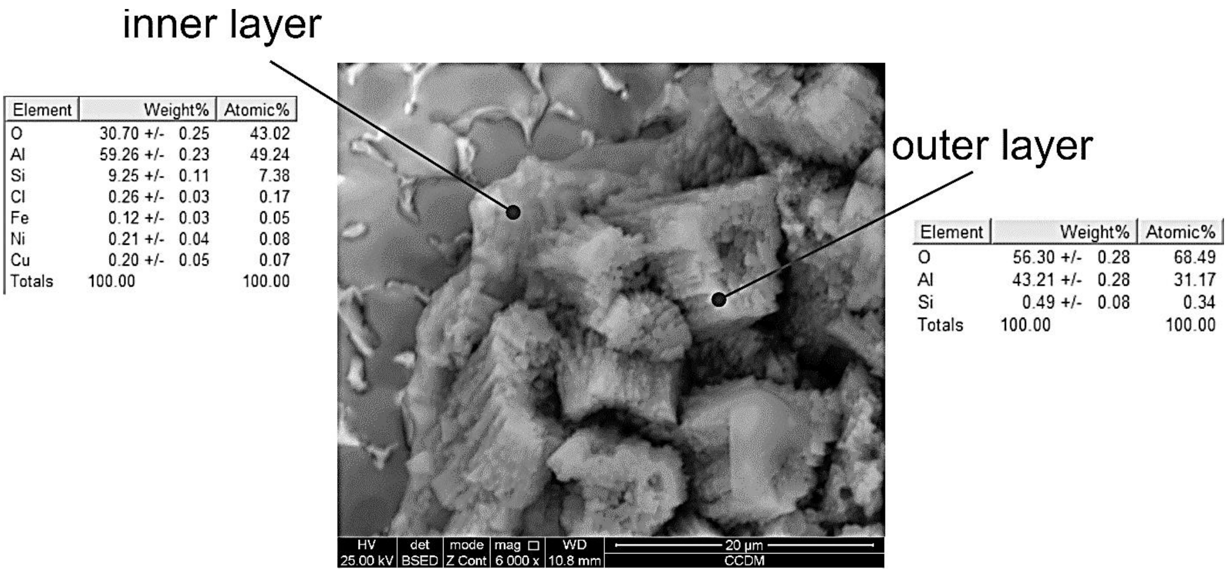

Element	Weight%	Atomic%
O	30.70 +/- 0.25	43.02
Al	59.26 +/- 0.23	49.24
Si	9.25 +/- 0.11	7.38
Cl	0.26 +/- 0.03	0.17
Fe	0.12 +/- 0.03	0.05
Ni	0.21 +/- 0.04	0.08
Cu	0.20 +/- 0.05	0.07
Totals	100.00	100.00

Element	Weight%	Atomic%
O	56.30 +/- 0.28	68.49
Al	43.21 +/- 0.28	31.17
Si	0.49 +/- 0.08	0.34
Totals	100.00	100.00

Figure 13. EDS measurements related to the inner and outer oxide layers formed during 30-day immersion experiments of the CC Al-7%Si-0.6%Fe-0.35%Cu-0.25%Zn-0.5%Ni alloy.

4. Conclusions

In this study, the microstructure formation and corrosion behavior of as-cast Co and Ni containing Al-Si-based alloys were investigated, and the following findings were reached:

- The microstructures of the alloys were formed by the α-Al dendritic matrix, Si and AlFeSi / AlFeSi(Ni) / AlFeSi(Co) phases. The additions of either Co or Ni were not able to change the SDAS as compared to the non-modified alloy. The fast cooling process resulted in a reduction of SDAS of approximately 4 times.

- Considering the short elapsed time measurements, the currents associated with the E_{corr}, i.e. the corrosion current density (i_{corr}), appear to be highest for the Ni-containing alloy and lowest for the unmodified alloy. Although not applying the Taefl extrapolation, E_{corr} clearly demonstrates that the i_{corr} is more likely to be found at better levels ranging from 10^{-6} to 10^{-5} A/cm^2. Moreover, the resistance to anodic polarization was marginally higher in the CC non-modified and Co-containing alloys in comparison to the corresponding DS samples.
- EIS studies revealed that the Ni-containing alloy had lower surface layer and charger transfer resistances, confirming its worst resistance to corrosion as subjected to early (1-hour) exposure time to the 0.6 M NaCl.
- Due to the formation of a thick and dense alumina layer containing Ni in its inner layer, the Ni-containing alloy showed a lower corrosion rate under long exposure conditions (30-days). It is understood from the results of the present investigation that the addition of small amount of Ni may be beneficial for longer exposure times to the saline electrolyte.

Author Contributions: Methodology, G.Y.K.; investigation, G.Y.K., M.G.C.X., B.J.M.F.; data curation, M.G.C.X., B.J.M.F., writing—original draft preparation, M.G.C.X., J.E.S..; writing—review and editing, G.Y.K., J.E.S.; supervision, G.Y.K, J.E.S.; funding acquisition, J.E.S. All authors have read and agreed to the published version of the manuscript.

Funding: The authors are grateful to CNPq - National Council for Scientific and Technological Development, Brazil and to FAPESP - São Paulo Research Foundation, Brazil (grant: #2019/23673-7) for their financial support. This study was financed in part by the Coordenação de Aperfeiçoamento de Pessoal de Nível Superior - Brasil (CAPES) - Finance Code 001.

Data Availability Statement: Data presented in this study are available on request from the corresponding author. Data are not publicly available because pertain to a research still in development.

Conflicts of Interest: The authors declare no conflict of interest.

doi:10.20944/preprints202203.0212.v1

References

1. Kruger, J.; Lillard, R.S.; Streinz, C.C.; Moran, P.J. Effect of Microstructure on Passive Film Formation and Breakdown of Al-Ta Alloys. **1992**, 127–136.
2. Natishan, P. M.; Mccafferty, E.; Hubler, G.. Surface charge considerations in the pitting of ion-implanted aluminum. *J. Electrochem. Soc.* **1988**, *135*, 321–327.
3. Scully, J.R.; Knight, T.O.; Buchheit, R.G.; Peebles, D.E. Electrochemical characteristics of the Al2Cu, Al3Ta and Al3Zr intermetallic phases and their relevancy to the localized corrosion of Al alloys. *Corros. Sci.* **1993**, *35*, 185–195.
4. Birbilis, N.; Buchheit, R.G. Electrochemical Characteristics of Intermetallic Phases in Aluminum Alloys An Experimental Survey and Discussion. **2005**, 140–151, doi:10.1149/1.1869984.
5. Brown, G.M.; Shimizu, K.; Kobayashi, K.; Thompson, G.E.; Wood, G.C. The growth of chromate conversion coatings on high purity aluminium. *Corros. Sci.* **1993**, *34*, 1045–1054.
6. Shimizu, K., Brown, G., Kobayashi, K., Skeldon, P., Thompson, G., & Wood, G. Ultramicrotomy—a route towards the enhanced understanding of the corrosion and filming behaviour of aluminium and its alloys. *Corros. Sci.* **1998**, *40*, 1049–1072.
7. Ezuber, H.; El-Houd, A.; El-Shawesh, F. Materials & Design A study on the corrosion behavior of aluminum alloys in seawater. *Mater. Des.* **2008**, *29*, 801–805, doi:10.1016/j.matdes.2007.01.021.
8. Meng, G.; Wei, L.; Zhang, T.; Shao, Y.; Wang, F.; Dong, C.; Li, X. Effect of microcrystallization on pitting corrosion of pure aluminium. *Corros. Sci.* **2009**, *51*, 2151–2157, doi:10.1016/j.corsci.2009.05.046.
9. Kaiser, M.S.; Sabbir, S.H.; Rahman, M.; Kabir, M.S.; Nur, M. Al Effect of Fe, Ni and Cr on the corrosion behavior of hypereutectic Al-Si automotive alloy in 3.5% NaCl solution at different temperature and velocity. *Mech. Eng.* **2018**, *ME48*, 11–17.
10. Hossain, A.; Gulshan, F.; Syed, A.; Kurny, W. Electrochemical corrosion behavior of Ni-containing hypoeutectic Al-Si alloy. *Electrochem. Sci.* **2015**, *5*, 173–179, doi:10.5599/jese.174.
11. Sani A. S., Aliyu I., P.E. Effect of Chromium and Cobalt Additions on the Corrosion Resistance of Aluminium Silicon Iron Alloy (Al-Si- Fe). *J. Sci. Eng. Res.* **2012**, *3*.
12. Mirzaee-Moghadam, M.; Lashgari, H.R.; Zangeneh, S.; Rasaee, S.; Seyfor, M.; Asnavandi, M.; Mojtahedi, M. Dry sliding wear characteristics, corrosion behavior, and hot deformation properties of eutectic Al–Si piston alloy containing Ni-rich intermetallic compounds. *Mater. Chem. Phys.* 2022, *279*, 125758.
13. Arthanari, S.; Jang, J.C.; Shin, K.S. Corrosion studies of high pressure die-cast Al-Si-Ni and Al-Si-Ni-Cu alloys. *J. Alloys Compd.* **2018**, *749*, 146–154, doi:10.1016/j.jallcom.2018.03.246.
14. Osório WR, Cheung N, Spinelli JE, Cruz KS, G.A. Microstructural modification by laser surface remelting and its effect on the corrosion resistance of an Al – 9 wt % Si casting alloy. **2008**, *254*, 2763–2770, doi:10.1016/j.apsusc.2007.10.013.
15. Xavier, M.G.C.; Freitas, B.J.M.; Gouveia, G.L.; Garcia, A.; Spinelli, J.E. The Roles of Ni and Co in Dendritic Growth and Tensile Properties of Fe-Containing Al–Si–Cu–Zn Scraps under Slow and Fast Solidification Cooling. *Adv. Eng. Mater.* **2021**, *2100822*, 1–16, doi:10.1002/adem.202100822.
16. Silva, B. L., Cheung, N., Garcia, A., Spinelli, J.E. Thermal Parameters, Microstructure, and Mechanical Properties of Directionally Solidified Sn-0.7 wt.%Cu Solder Alloys Containing 0 ppm to 1000 ppm Ni. *J. Electron. Mater.* **2013**, *42*, 179–191, doi:10.1007/s11664-012-2263-7.
17. Sivarupan, T.; Taylor, J.A.; Cáceres, C.H. SDAS, Si and Cu Content, and the Size of Intermetallics in Al-Si-Cu-Mg-Fe Alloys. *Metall. Mater. Trans. A Phys. Metall. Mater. Sci.* **2015**, *46*, 2082–2107, doi:10.1007/s11661-015-2808-5.
18. Xavier, M.G.C.; Souza, T.M.G.; Cheung, N.; Garcia, A.; Spinelli, J.E. Effects of cobalt and solidification cooling rate on intermetallic phases and tensile properties of a -Cu, -Zn, -Fe containing Al-Si alloy. *Int. J. Adv. Manuf. Technol.* **2020**, *107*, 717–730, doi:10.1007/s00170-020-05077-4.
19. Žihalová, M.; Bolibruchová, D.; Matejka, M. Change in the microstructure of alsi10mgmn alloy with higher iron content due to an increase in the amount of nickel. *Teh. Vjesn.* **2021**, *28*, 34–37, doi:10.17559/TV-20150513155430.

20. Silva, A.P.; Spinelli, J.E.; Mangelinck-noël, N.; Garcia, A. Microstructural development during transient directional solidification of hypermonotectic Al – Bi alloys. *Mater. Des.* **2010**, *31*, 4584–4591, doi:10.1016/j.matdes.2010.05.046.
21. Vandersluis, E.; Lombardi, A.; Ravindran, C.; Bois-brochu, A.; Chiesa, F.; Mackay, R. Materials Science & Engineering A Factors in fl uencing thermal conductivity and mechanical properties in 319 Al alloy cylinder heads. *Mater. Sci. Eng. A* **2015**, *648*, 401–411, doi:10.1016/j.msea.2015.09.091.
22. Gündüz, M., Çadirli, E. Directional solidification of aluminium – copper alloys. *Mater. Sci. Eng. A* **2002**, *327*, 167–185.
23. Mansfeld, F.; Fernandes, J.C.S. Impedance spectra for aluminum 7075 during the early stages of immersion in sodium chloride. *Corros. Sci.* **1993**, *34*, 2105–2108, doi:10.1016/0010-938X(93)90063-M.
24. Moreto, J.A.; dos Santos, M.S.; Ferreira, M.O.A.; Carvalho, G.S.; Gelamo, R. V.; Aoki, I. V.; Taryba, M.; Bose Filho, W.W.; Fernandes, J.C.S. Corrosion and corrosion-fatigue synergism on the base metal and nugget zone of the 2524-T3 Al alloy joined by FSW process. *Corros. Sci.* **2021**, *182*, 109253, doi:10.1016/j.corsci.2021.109253.
25. Moreto, J.A.; Rossino, L.S.; Filho, W.W.B.; Marino, C.E.B.; Da Conceição Ferreira, M.; Taryba, M.; Fernandes, J.C.S. On the global and localised corrosion behaviour of the AA2524-T3 aluminium alloy used as aircraft fuselage skin. *Mater. Res.* **2019**, *22*, doi:10.1590/1980-5373-MR-2018-0280.
26. Moreto, J.A.; Gelamo, R. V.; Nascimento, J.P.L.; Taryba, M.; Fernandes, J.C.S. Improving the corrosion protection of 2524-T3-Al alloy through reactive sputtering Nb2O5 coatings. *Appl. Surf. Sci.* **2021**, *556*, 149750, doi:10.1016/j.apsusc.2021.149750.
27. ASTM Standard guide for laboratory immersion corrosion testing of metals. *ASTM Int.* **2012**, *G31-12a*, 1–10, doi:10.1520/G0031-12A.
28. Zhang, Z.; Liu, M.-Y.; Breton, F.; Chen, X.-G. Microstructure and Mechanical Properties of AlSi10Mg Permanent Mould and High Pressure Vacuum Die Castings. In Proceedings of the 16th International Aluminum Alloys Conference (ICAA16); 2018; p. 399716.
29. Yan, Q.; Song, B.; Shi, Y. Comparative study of performance comparison of AlSi10Mg alloy prepared by selective laser melting and casting. *J. Mater. Sci. Technol.* **2020**, *41*, 199–208, doi:10.1016/j.jmst.2019.08.049.
30. Hwang, J.Y.; Doty, H.W.; Kaufman, M.J. The effects of Mn additions on the microstructure and mechanical properties of Al-Si-Cu casting alloys. *Mater. Sci. Eng. A* **2008**, *488*, 496–504, doi:10.1016/j.msea.2007.12.026.
31. Arthanari, S.; Jang, J.C.; Shin, K.S. Corrosion Behavior of High Pressure Die Cast Al-Ni and Al-Ni-Ca Alloys in 3.5% NaCl Solution. *Corros. Sci. Technol.* **2017**, *3*, 100–108.
32. Martin, F.J.; Cheek, G.T.; O'Grady, W.E.; Natishan, P.M. Impedance studies of the passive film on aluminium. *Corros. Sci.* **2005**, *47*, 3187–3201, doi:10.1016/j.corsci.2005.05.058.
33. Osório, W.R.; Goulart, P.R.; Garcia, A. Effect of silicon content on microstructure and electrochemical behavior of hypoeutectic Al–Si alloys. *Mater. Lett.* **2008**, *62*, 365–369, doi:10.1016/j.matlet.2007.05.051.
34. Das, N.; Sengupta, P.; Abraham, G.; Arya, A.; Kain, V.; Dey, G.K. Development in corrosion resistance by microstructural refinement in Zr-16 SS 304 alloy using suction casting technique. *Mater. Res. Bull.* **2016**, *80*, 295–302, doi:10.1016/j.materresbull.2016.04.016.
35. Christian Vargel *Corrosion of Aluminium*; 2020; ISBN 9780080999258.
36. Roche, V.; Koga, G.Y.; Matias, T.B.; Kiminami, C.S.; Bolfarini, C.; Botta, W.J.; Nogueira, R.P.; Jorge Junior, A.M. Degradation of biodegradable implants: The influence of microstructure and composition of Mg-Zn-Ca alloys. *J. Alloys Compd.* **2019**, *774*, 168–181, doi:10.1016/j.jallcom.2018.09.346.